IEEE Access
Multidisciplinary | Rapid Review | Open Access Journal

Received September 16, 2021, accepted September 21, 2021, date of publication September 23, 2021,
date of current version October 4, 2021.

Digital Object Identifier 10.1109/ACCESS.2021.3115359

System Modeling and Motion Control of a Cable-Driven Parallel Platform for Underwater Camera Stabilization

ZHIQI ZHAO, LEI ZHANG, HAIJIAO NAN, AND BINBIN WANG
School of Physics and Electronics, Henan University, Kaifeng 475004, China

Corresponding author: Lei Zhang (zhanglei@vip.henu.edu.cn)

This work was supported in part by the National Natural Science Foundation of China under Grant 61773008, and in part by Henan Province Young Key Teacher under Grant 2019GGJS032.

ABSTRACT Underwater camera platform's low image stabilization accuracy and poor waterproofness seriously restrict the quality of photos. In order to better cope with underwater camera work, this paper proposes a cable-driven underwater camera stabilized platform. It is a mobile platform driven in parallel by four flexible cables. To improve image stabilization accuracy and anti-interference performance, the system's dynamic model is established in a non-inertial reference frame. And the random water wave interference is modeled. Moreover, a novel double-loop integral-type global fast terminal sliding mode control strategy is designed. Lyapunov stability theory is used to analyze the stability of the strategy. Finally, by comparing with the existing global fast terminal sliding mode controller and traditional sliding mode controller, the designed controller is simulated and verified. The results show that the proposed control strategy not only has the advantages of fast response and robustness, but also has the characteristics of rapid convergence in a finite time and high accuracy. This method can provide a valuable reference for the development of underwater camera stabilized platforms.

INDEX TERMS Cable-driven parallel robot, dynamic model, global fast terminal sliding mode control, underwater stabilized platform.

I. INTRODUCTION

With the development of underwater scientific exploration, underwater photography has become an indispensable work [1]. Underwater camera stabilized platform (UCSP) has a wide range of application values, such as the stable tracking and shooting of underwater creatures through cameras installed on the UCSP [2], [3]. Besides, it can be applied to video surveillance of marine ecological protection areas, and the camera attitude can be adjusted through the UCSP to achieve the goal of stable shooting in a specific direction and area [4]. In order to track the image of the target stably, the camera device needs to adjust the shooting angle along with the movement of the target. Camera stabilized platform (CSP) is a device that can keep the camera stable under external interference and can move according to a desired law. The camera should complete the three-degree-of-freedom (3-DOF) rotation movement in space under the effect of CSP to ensure that the shooting angle can be adjusted at any time to achieve the purpose of stable shooting. Due to the considerations of underwater environments, device waterproofing issues, and external interference, underwater photography is a relatively complex application scenario for CSP.

In recent years, for different application purposes, cable-driven robots have been extensively studied by researchers and engineers. A variety of cable-driven robot application design solutions have been proposed, such as in the field of aerial robots [5], [6], human rehabilitation movement [7], [8], and marine platforms [9], [10]. In addition, due to the need of underwater work, the application of underwater robots in marine industry and marine scientific research has become more and more extensive. Literature [10] proposed a Gough-Stewart type cable marine platform and studied its workspace under the action of harmonic water waves. Literature [11] proposed an underwater manipulator driven by a hybrid of cables and drivers, and studied its force-bearing capabilities. Debruyn *et al.* [12] proposed an Aerial-aquatic dual robot for the purpose of automatic

The associate editor coordinating the review of this manuscript and approving it for publication was Mohammad Alshabi.

collection of underwater samples in complex areas, focusing on its mechanical design and control method. Horoub and Hawwa [13] analyzed the cable distribution characteristics of the parallel robot ocean platform, focusing

on the influence of cable distribution on the platform's dynamic characteristics and workspace.

However, there are few related researches on UCSP. To deal with the lack of image stabilization accuracy, poor waterproofness of traditional robot platforms, and complex underwater camera environment, this paper designs a novel type of cable-driven underwater camera stabilized platform (CDUCSP). The designed CDUCSP belongs to the field of cable-driven parallel robots (CDPR), which replaces rigid links with multiple flexible cables, which effectively reduces the platform's motion inertia and expands the workspace [14]–[16]. In addition, the heavy driving device is placed in the base, so that the driving device and the mobile platform are separated, which effectively decreases difficulties in waterproofness and is more suitable for underwater work. The current work mainly focuses on the mechanism design, dynamic modeling, controller design, and simulation verification of the CDUCSP.

Because the CDPR system has the characteristics of nonlinearity and strong coupling, it is challenging to model it accurately. The modeling process consistently produces a set of highly coupled nonlinear equations. Dynamic modeling of CDPR is a prerequisite for motion control. And dynamic analysis can optimize model design and improve control performance [17]. For the complex dynamic modeling of CDPR, people have conducted in-depth research [18]–[20]. The typical dynamic modeling methods are Newton-Euler method, Lagrange method, Kane method, and virtual work method [21]–[23]. Among them, the Newton-Euler method is more suitable for modeling complex CDPR because of its convenient modeling and high accuracy. Caverly and Forbes [24] deduced the dynamic model of a flexible planar cable-driven manipulator through the Lagrangian derivation of a lumped-mass cable model in two dimensions and the null-space method. This method explicitly takes into account the change in cable stiffness and winch inertia when the cables are wound around their respective winches. Jamshidifar *et al*. [25]–[27] have conducted much research on the undesired vibration problem of the end-effector and cable of cable-driven parallel robots and achieved important research results. These studies put forward the idea of using actuators to suppress the undesired vibration of CDPRs. On this basis, when the proposed stabilizer can regulate all undesired vibrations of the system, the issue of the minimum number of required actuators is further studied. However, in view of the irregular movement of the robot's carrier over time, most researchers ignore the influence of the carrier's movement [11], [12]. Considering the influence of carrier's movement on the end-effector, the mobile platform in a non-inertial reference frame is modeled in detail. On this basis, a precise dynamic model of CDUCSP is established by Newton-Euler method.

Quickly obtaining the cable's tension and keeping the tension within a reasonable range are the key to robot motion control, so research on the tension solution algorithm is necessary. In [28] and [29], a method of optimizing cable tension using P-norm is proposed, which solves the real-time problem of cable tension. However, it is easy to cause discontinuity of cable tension during movement. Borgstrom *et al.* [30] proposed the ''optimally safe'' tension distribution method to avoid the phenomenon of cable tension relaxation. However, the proposed algorithm takes too long to calculate the tension, which affects the real-time control performance of the robot. Caverly and Forbes [31] used a strictly positive real controller to control planar cable-driven parallel manipulator, which explicitly considered the cable pretension and avoided the cable slack. The controller can track high acceleration trajectories while maintaining positive cable tensions. El-Ghazaly *et al*. [32] proposed an extended adaptive control scheme via terminal sliding mode for cable-driven parallel manipulators. Redundancy resolution is solved based on the limits on control input torques corresponding to the tension limits. The controller realizes that cable tensions are within a non-negative range of admissible values during the control process. In this paper, a non-iterative tension solution algorithm is studied, which can solve the cable tension within a reasonable time, and it is easier to achieve real-time performance. It uses the Moore-Penrose pseudoinverse of Jacobian matrix to calculate the cable tension and maintain continuity, which can meet the tension solution requirements of the designed CDUCSP.

The CDPR is a multi-variable, nonlinear, and strongly coupled system with uncertainty and interference. It is imperative to design a suitable controller to reduce system motion errors and enhance image stabilization accuracy and robustness [33], [34]. In order to obtain better control performance, many control strategies have been applied to CDPR systems, including fuzzy control [35], neural network control [36], robust control [37], and sliding mode control (SMC) [38]. Among them, SMC has been widely studied for its easy design, strong robustness and fast response speed [39]–[42]. However, the control law of traditional SMC is discontinuous, which leads to chattering and reduces system performance. In addition, when the system is affected by rapid changes in disturbances, traditional SMC cannot converge in a finite time. In order to reduce the chattering phenomenon, people have proposed to weaken it with the method of reaching law. [43], [44]. The reaching law method can directly deal with the arrival process at the sliding mode surface. By adjusting the reaching law parameters, it can not only ensure the dynamic quality of the sliding mode arrival process, but also reduce chattering [45]. The commonly used methods of reaching law include isokinetic reaching law, exponential reaching law, and power reaching law [46]. Meanwhile, in order to solve the finite time convergence problem, people have proposed terminal SMC (TSMC) [47], [48] and fast TSMC (FTSMC) [49], [50]. TSMC is a nonlinear sliding mode surface, which enhances the dynamic convergence

characteristics of the system while guaranteeing finite time convergence. Compared with TSMC, when the state deviation variable is far from the equilibrium point, FTSMC has a faster convergence speed. Based on the FTSMC, a new concept of global FTSMC (GFTSMC) was proposed [51]. GFTSMC ensures that the system state converges to the equilibrium state more quickly within a finite time. At the same time, because the control law is continuous and does not include switching items, it can effectively eliminate system chattering. Furthermore, GFTSMC has also been extensively studied in robot control [52]–[54]. Therefore, GFTSMC based on the reaching law will effectively improve the performance of sliding mode control.

Based on the above analysis, combined with the improved sliding mode surface and reaching law, a novel double-loop integral-type GFTSMC (DIGFTSMC) control strategy is proposed. It consists of an attitude loop and an angular velocity loop, which are used to track the desired attitude and angular velocity of the CDUCSP, respectively. In addition, by modeling the inertial torque, the obtained compensation torque is applied to the DIGFTSMC design. The uncertainty of the model is further weakened, and the control performance of DIGFTSMC is improved. At the same time, the integral function is used to realize the design of the sliding mode surface, and an exponential function is used for the design of the reaching law. Therefore, compared with the existing GFTSMC [55] and the traditional SMC [56], the proposed DIGFTSMC has the advantages of fast response and robustness and has the characteristics of rapid convergence in finite time and small stable tracking error. The specific contributions are summarized as:

(1) This paper proposes a novel type of CDUCSP. It is driven by cables to move the mobile platform, and all heavier driving devices are placed in the base. Compared with the traditional serial and parallel rigid robot platform, the device has strong waterproof performance, large structural rigidity, small overall inertia, and strong load capacity, which is more suitable for underwater camera environments.

(2) To eliminate the influence of carrier's movement on the platform as much as possible, the overall dynamic model of CDUCSP is established in a non-internal system. Furthermore, in order to verify the anti-interference characteristics, the random water wave interference is modeled in detail.

(3) A new type of DIGFTSMC control strategy is proposed. The simulation results show that compared with the existing GFTSMC and SMC, DIGFTSMC has the advantages of fast finite time convergence, high tracking accuracy, fast transient response, and strong robustness.

The rest of the paper is arranged as follows. Section II introduces the mechanical design of CDUCSP in detail; Section III establishes the CDUCSP kinematic and dynamic models, and models the random disturbance of water wave and inertial torque; In section IV, the DIGFTSMC control strategy and cable tension solution algorithm are designed; Section V makes simulations of CDUCSP under the two sets of motion laws and random water wave interference; Section VI draws the conclusions and describes some future works.

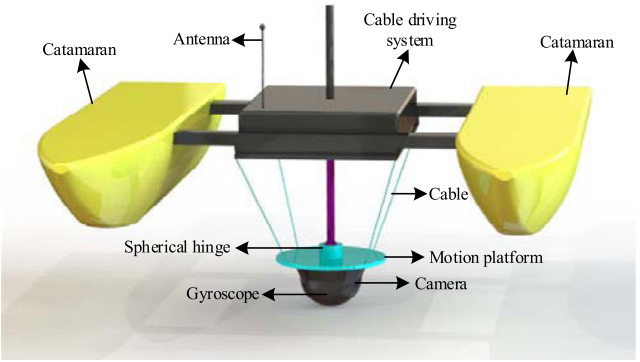

FIGURE 1. CDUCSP mechanical structure.

II. MECHANICAL DESIGN

A. MECHANICAL STRUCTURE

The overall mechanical structure is shown in Fig. 1. The CDUCSP is composed of catamaran, cable driving system, camera, antenna, and 3-DOF parallel platform.

The catamaran comprises two yellow hulls and two black fixed rods, which serve as the carrier of the entire platform system in the water. The cable driving system is composed of heavier servo motor and reducer, and is covered by a black shell. It is placed on the black bracket of the catamaran and is separated from the water surface, which is beneficial to improve the overall waterproofness of the CDUCSP. And the cable driving system has a gyroscope and accelerometer inside. There is a black cylindrical hollow shell at the top, and the purpose is to shrink the purple cylindrical rod of the 3-DOF parallel platform to the top when the CDUCSP is idle. The 3-DOF parallel platform is composed of base, mobile platform, restraint mechanism, and four cables. The cable connects the mobile platform and the base, and the restraint mechanism is composed of spherical hinge. One end of the spherical hinge is fixedly connected with the base, and the other end is connected with the mobile platform. The translation of the platform is restricted, so that the mobile platform can only rotate in three dimensions along the center point of the spherical hinge. The attitude angle is controlled by the cable tension. The camera is used to take video or image. A gyroscope and accelerometer are installed on the mobile platform, which can detect the angular velocity and angular acceleration of the end-effector (the mobile platform and the upper part of the spherical hinge) in real-time. The antenna is used for wireless communication with the ground station.

B. PLATFORM FRAMEWORK

In order to facilitate modeling, the mechanical structure model of CDUCSP can be simplified to the 3-DOF parallel robot platform model. The reference frames and the associated motion parameters of CDUCSP are shown in Fig. 2.

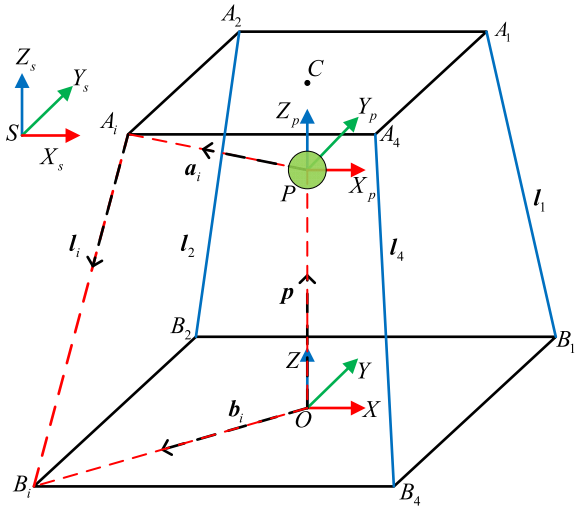

FIGURE 2. Reference frames and motion parameters of CDUCSP.

As shown in Fig. 2, the kinematics symbol of CDUCSP is defined. The inertial coordinate frame is denoted as $\{S\}$, the catamaran coordinate frame is denoted as $\{O\}$, the platform coordinate frame is denoted as $\{P\}$. The origin O of the frame $\{O\}$ is fixed at the catamaran, and the origin P of the frame $\{P\}$ is fixed at the center of the spherical joint. ${}^o\boldsymbol{l}_i = \overrightarrow{A_iB_i}(i = 1, 2, 3, 4)$ is the direction vector of the i-th cable in the frame $\{O\}$. ${}^p\boldsymbol{a}_i = \overrightarrow{PA_i}$ $(i = 1, 2, 3, 4)$ is the position vector from point P to the connection point between the i-th cable and end-effector in the frame $\{P\}$. ${}^o\boldsymbol{b}_i = \overrightarrow{OB_i}$ $(i = 1, 2, 3, 4)$ is the position vector from O to the connection point between the i-th cable and the base in the frame $\{O\}$. ${}^o\boldsymbol{p} = \overrightarrow{OP}$ is the position vector of the origin P in the frame $\{O\}$. It can be seen from the set coordinate system that the vectors ${}^o\boldsymbol{b}_i$, ${}^o\boldsymbol{p}$, ${}^p\boldsymbol{a}_i$ are constants. C is the center of mass of the end-effector. ${}^p\boldsymbol{r} = \overrightarrow{PC}$ is the position vector in the frame $\{P\}$. ${}^o\boldsymbol{r} = \overrightarrow{OC}$ is the position vector in the frame $\{O\}$.

III. MODELING ANALYSIS

A. KINEMATICS

Kinematics analysis is a prerequisite for the robot to complete trajectory planning and system control. $\boldsymbol{\theta} = [\alpha\ \beta\gamma]^T$ is the attitude angle of the end-effector. α, β, and γ respectively denotes the Euler angle, which are transformed by the $Z-Y-X$ transformation principle. ${}^o_p\boldsymbol{R}$ is the rotation matrix from the frame $\{P\}$ to the frame $\{O\}$, expressed as

$$ {}^o_p\boldsymbol{R} = \begin{bmatrix} c\gamma c\beta c\gamma & s\beta s\alpha - s\gamma c\alpha & c\gamma s\beta c\alpha + s\gamma s\alpha \\ s\gamma c\beta & s\gamma s\beta s\alpha + c\gamma c\alpha & s\gamma s\beta c\alpha - c\gamma s\alpha \\ -s\beta & c\beta s\alpha & c\beta c\alpha \end{bmatrix} \tag{1} $$

where c is represented as 'cos', s is represented as 'sin'.

According to Fig. 2, by the principle of space vector transformation

$$ {}^o\boldsymbol{l}_i = {}^o\boldsymbol{b}_i - {}^o\boldsymbol{p} - {}^o\boldsymbol{a}_i, i = 1, 2, 3, 4 \tag{2} $$

$$ {}^o\boldsymbol{a}_i = {}^o_p\boldsymbol{R}\,{}^p\boldsymbol{a}_i \tag{3} $$

Combining Eq. (2) with Eq. (3), we have

$$ {}^o\boldsymbol{l}_i = {}^o\boldsymbol{b}_i - {}^o\boldsymbol{p} - {}^o_p\boldsymbol{R}\,{}^p\boldsymbol{a}_i, \quad i = 1, 2, 3, 4 \tag{4} $$

The length of the i-th cable can be expressed as

$$ {}^o l_i = \left\| {}^o\boldsymbol{l}_i \right\|, \quad i = 1, 2, 3, 4 \tag{5} $$

For CDUCSP, since the end-effector realizes rotation around three coordinate axes in space, the coordinate origin P of the frame $\{P\}$ is stationary relative to the frame $\{O\}$. The translational velocity and translational acceleration of the end-effector in the frame $\{P\}$ are zero, and only the rotation velocity and the rotation acceleration of the end-effector change. The linear transformation between the rotation velocity of the CDUCSP end-effector and the change rate of cable length is defined as the motion Jacobian matrix of CDUCSP. The motion Jacobian matrix can be obtained by deriving the inverse solution of the robot's velocity. Let

$$ \boldsymbol{\omega}_p = \left[\omega_{px}\omega_{py}\ \omega_{pz}\right]^T = \boldsymbol{J}_P^{-1}\dot{\boldsymbol{\theta}} \tag{6} $$

$$ \boldsymbol{\omega}_o = \left[\omega_x\omega_y\omega_z\right]^T = {}^o_p\boldsymbol{R}\boldsymbol{\omega}_p \tag{7} $$

where $\boldsymbol{J}_p = \begin{bmatrix} 1 & \sin\alpha\tan\beta & \cos\alpha\tan\beta \\ 0 & \cos\alpha & -\sin\alpha \\ 0 & \sin\alpha/\cos\beta & \cos\alpha/\cos\beta \end{bmatrix}$, $\boldsymbol{\omega}_p$ is the angular velocity vector of the end-effector in the frame $\{P\}$, $\boldsymbol{\omega}_o$ is the angular velocity vector of the end-effector in the frame $\{O\}$, $\boldsymbol{u}_i$ is the unit vector of the i-th cable, and its direction is the same as the direction of the cable vector, which can be written as

$$ \boldsymbol{u}_i = {}^o\boldsymbol{l}_i \big/ \left\| {}^o\boldsymbol{l}_i \right\|, \quad i = 1, 2, 3, 4 \tag{8} $$

Since the vectors ${}^o\boldsymbol{b}_i$, ${}^o\boldsymbol{p}$, ${}^p\boldsymbol{a}_i$ are constants, so

$$ \frac{d}{dt}{}^o\boldsymbol{b}_i = 0, \ \frac{d}{dt}{}^o\boldsymbol{p} = 0, \ \frac{d}{dt}{}^p\boldsymbol{a}_i = 0 \tag{9} $$

From the derivative formula of the robot rotation matrix

$$ \frac{d}{dt}{}^o_p\boldsymbol{R} = \boldsymbol{\omega}_o \times {}^o_p\boldsymbol{R} \tag{10} $$

$$ \frac{d}{dt}({}^o_p\boldsymbol{R} \cdot {}^p\boldsymbol{a}_i) = \frac{d}{dt}{}^o_p\boldsymbol{R} \cdot {}^p\boldsymbol{a}_i = \boldsymbol{\omega}_o \times {}^o_p\boldsymbol{R} \cdot {}^p\boldsymbol{a}_i \tag{11} $$

Taking the derivation on both sides of Eq. (5), and substituting Eqs. (4), (9), (10), (11) into Eq. (5), we can get

$$ \begin{aligned} {}^o\dot{l}_i &= \frac{d}{dt}\left(\left\| {}^o\boldsymbol{l}_i \right\|\right) = \frac{1}{\left\| {}^o\boldsymbol{l}_i \right\|}\frac{d}{dt}\left(\frac{1}{2}\left\| {}^o\boldsymbol{l}_i \right\|^2\right) \\ &= \frac{1}{2\left\| {}^o\boldsymbol{l}_i \right\|}\frac{d}{dt}\left(\left\| {}^o\boldsymbol{b}_i - {}^o\boldsymbol{p} - {}^o_p\boldsymbol{R}\,{}^p\boldsymbol{a}_i \right\|^2\right) \\ &= \frac{1}{\left\| {}^o\boldsymbol{l}_i \right\|}\left[({}^o_p\boldsymbol{R}\,{}^p\boldsymbol{a}_i - {}^o\boldsymbol{b}_i + {}^o\boldsymbol{p}) \cdot \frac{d}{dt}({}^o_p\boldsymbol{R}\,{}^p\boldsymbol{a}_i)\right] \\ &= \frac{1}{\left\| {}^o\boldsymbol{l}_i \right\|}\left[-{}^o\boldsymbol{l}_i \cdot (\boldsymbol{\omega}_o \times {}^o_p\boldsymbol{R}\,{}^p\boldsymbol{a}_i)\right] \\ &= -\frac{1}{\left\| {}^o\boldsymbol{l}_i \right\|}\left[({}^o_p\boldsymbol{R}\,{}^p\boldsymbol{a}_i \times {}^o\boldsymbol{l}_i) \cdot \boldsymbol{\omega}_o\right] \\ &= -({}^o_p\boldsymbol{R}\,{}^p\boldsymbol{a}_i \times \boldsymbol{u}_i)^T \cdot \boldsymbol{\omega}_o \end{aligned} \tag{12} $$

where ${}^{o}\dot{l}_i (i = 1, 2, 3, 4)$ is the length change velocity of the i-th cable. The relationship between the change rate of cable length and the angular velocity of the end-effector is

$$\dot{\boldsymbol{l}} = -\boldsymbol{J}\boldsymbol{\omega}_o \tag{13}$$

where $\dot{\boldsymbol{l}}$ is the change rate vector of cable length. $\boldsymbol{J}$ is the motion Jacobian matrix of CDUCSP. They are represented by the following equations

$$\dot{\boldsymbol{l}} = \left[{}^{o}\dot{l}_1\, {}^{o}\dot{l}_2\, {}^{o}\dot{l}_3\, {}^{o}\dot{l}_4\right]^T_{4\times 1} \tag{14}$$

$$\boldsymbol{J} = \begin{bmatrix} ({}^{o}_{p}\boldsymbol{R}^{p}\boldsymbol{a}_1 \times \boldsymbol{u}_1) \\ ({}^{o}_{p}\boldsymbol{R}^{p}\boldsymbol{a}_2 \times \boldsymbol{u}_2) \\ ({}^{o}_{p}\boldsymbol{R}^{p}\boldsymbol{a}_3 \times \boldsymbol{u}_3) \\ ({}^{o}_{p}\boldsymbol{R}^{p}\boldsymbol{a}_4 \times \boldsymbol{u}_4) \end{bmatrix}_{4\times 3} \tag{15}$$

B. DYNAMICS

The dynamic model is the theoretical basis for the robot to realize the motion control. Using the Newton-Euler method [57], the dynamic equation of the end-effector is established in the frame $\{P\}$.

Translational dynamic equation:

$$0 = \sum_{i=1}^{4} t_i\boldsymbol{u}_i + m\boldsymbol{g} + \boldsymbol{F}_q + \boldsymbol{F}_e + \boldsymbol{F}_s \tag{16}$$

Rotational dynamic equation:

$$\boldsymbol{I}_p\dot{\boldsymbol{\omega}}_p + \boldsymbol{\omega}_p \times (\boldsymbol{I}_p\boldsymbol{\omega}_p) = \boldsymbol{M}_p + \boldsymbol{M}_g + \boldsymbol{M}_e + \boldsymbol{M}_s \tag{17}$$

$$\boldsymbol{M}_p = \sum_{i=1}^{4} ({}^{p}\boldsymbol{a}_i \times t_i\boldsymbol{u}_i) \tag{18}$$

$$\boldsymbol{M}_g = ({}^{p}\boldsymbol{r} \times m\boldsymbol{g}) \tag{19}$$

where m is defined as the mass of the end-effector, $\boldsymbol{M}_p$ is the total torque of the four cables acting on the end-effector in the frame $\{P\}$. $\boldsymbol{M}_g$ is the torque of gravity acting on the end-effector in the frame $\{P\}$. $\boldsymbol{F}_e$ and $\boldsymbol{M}_e$ are the sum of the interference force and torque of random water wave acting on the end-effector and the interference force and torque caused by cable elasticity, respectively. $\boldsymbol{F}_s$ and $\boldsymbol{M}_s$ are the inertial force and torque of catamaran acting on the end-effector, respectively. $\boldsymbol{F}_q$ is the force of the spherical hinge on the end-effector, $\boldsymbol{g} = [00 - 9.8]^T$ m/s^2 is the gravity acceleration vector, $\boldsymbol{I}_p = \begin{bmatrix} I_{xx} & -I_{xy} & -I_{xz} \\ -I_{yx} & I_{yy} & -I_{yz} \\ -I_{zx} & -I_{zy} & I_{zz} \end{bmatrix}$ is the inertia tensor of the end-effector in the frame $\{P\}$.

Since the origin P of the frame $\{P\}$ is stationary relative to the frame $\{O\}$, only the rotational dynamic equation is considered. From Eq. (17), the dynamic equation of CDUCSP can be further written

$$\boldsymbol{J}^T\boldsymbol{T} = \boldsymbol{M}_p + \boldsymbol{M}_g + \boldsymbol{M}_e + \boldsymbol{M}_s \tag{20}$$

where, $\boldsymbol{T} = [t_1 t_2 t_3 t_4]^T$ is the tension of the four cables.

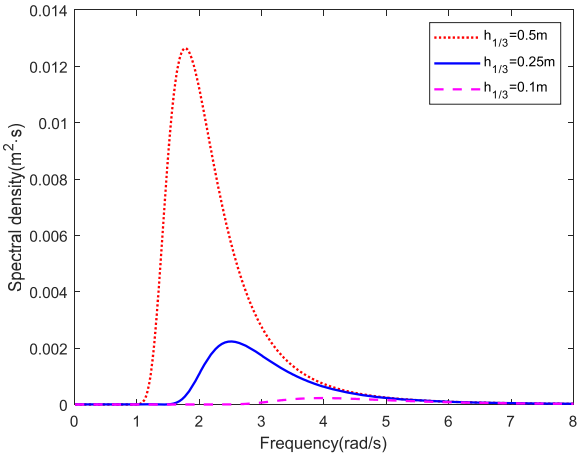

FIGURE 3. P-M spectrum under different wave heights.

C. RANDOM WATER WAVE INTERFERENCE

Water waves can be regarded as a random process composed of countless cosine waves with different amplitudes, frequencies, and random initial phases. The corresponding general wave surface function can be written as

$$\zeta(t) = \sum_{i=1}^{n} \zeta_{ai}\cos(\omega_{ai}t + \varepsilon_i) \tag{21}$$

where $\zeta(t)$ is the instantaneous height of the fluctuating water surface relative to the static water surface, ζ_{ai} and ω_{ai} represent the amplitude and circular frequency of the i-th component wave, ε_i is a random variable within $(0, 2\pi)$, which represents the initial phase of the i-th component wave.

In order to determine the amplitude and circular frequency of each component wave, this paper adopts the P-M spectrum as the simulated water wave spectrum function [58], and its form is as follows

$$S_\zeta(\omega_a) = \frac{A}{\omega_a^5}\exp\left(-\frac{B}{\omega_a^4}\right) \tag{22}$$

where $A = 8.11 \times 10^{-3}g^2$, $B = 3.11\Big/h_{1/3}^2$, g is the accelera-tion of gravity, $h_{1/3}$ is the significant wave height, ω_a is the frequency of water wave.

When $h_{1/3}$ is 0.5m, 0.25m, and 0.1m respectively, the spectral density function is shown in Fig. 3.

The water wave amplitude obtained according to the equal-time discrete method [58] is

$$\zeta_{ai} = \sqrt{2S_\zeta(\omega_{ai})\Delta\omega_a} \tag{23}$$

where $\Delta\omega_a$ represents the interval of the sampling frequency. The slicing method is used to obtain the interference torque of water waves acting on CDUCSP at different frequency points, and the interference torque of random water waves acting on end-effector can be obtained by the method of linear superposition [59].

D. INERTIA TORQUE

Since the base of the 3-DOF parallel platform is fixed on the catamaran, the movement of the catamaran in the water waves can cause non-negligible interference to the end-effector. Pitching, rolling, and heaving are the main swaying motions of the hull. Considering that the movement of catamaran has the most influence on the attitude of end-effector, this paper focuses on the interference of catamaran to the attitude of end-effector. The inertial torque generated by the catamaran to the end-effector when it is moving is calculated.

The inertial torque of catamaran acting on the end-effector is

$$\begin{aligned} \boldsymbol{M}_s &= -[\boldsymbol{I}_s({}^s_o\boldsymbol{a} + {}^o_p\boldsymbol{a}\boldsymbol{\mathcal{C}}\,{}^s_o\boldsymbol{\omega} \times \boldsymbol{\omega}_o) + {}^s_p\boldsymbol{\omega} \times (\boldsymbol{I}_s\,{}^s_p\boldsymbol{\omega})] \\ &\quad + {}^s_p\boldsymbol{R}^p\boldsymbol{r} \times \boldsymbol{F}_s \qquad (24) \\ \boldsymbol{F}_s &= -m[\boldsymbol{a}^c_o + \boldsymbol{a}^o_s + {}^s_o\boldsymbol{\omega} \times ({}^s_o\boldsymbol{\omega} \times {}^o\boldsymbol{r}) + {}^s_o\boldsymbol{a} \times {}^o\boldsymbol{r} \\ &\quad + 2{}^s_o\boldsymbol{\omega} \times (\boldsymbol{\omega}_o \times {}^p\boldsymbol{r})] \qquad (25) \\ {}^o\boldsymbol{r} &= {}^o_p\boldsymbol{\mathcal{C}}\,{}^o_p\boldsymbol{R}^p\boldsymbol{r} \qquad (26) \\ {}^s_p\boldsymbol{\omega} &= {}^s_o\boldsymbol{\omega} + \boldsymbol{\omega}_o \qquad (27) \\ {}^s_p\boldsymbol{R} &= {}^s_o\boldsymbol{R}\,{}^o_p\boldsymbol{R} \qquad (28) \end{aligned}$$

where, $\boldsymbol{a}^c_o$ is the acceleration of the center of mass C of the end-effector relative to the frame $\{O\}$, $\boldsymbol{a}^o_s$ is the acceleration of the origin O of the frame $\{O\}$ relative to the frame $\{S\}$, ${}^s_o\boldsymbol{\omega}$ is the angular velocity of the frame $\{O\}$ relative to the frame $\{S\}$, ${}^s_o\boldsymbol{a}$ is the angular acceleration of the frame $\{O\}$ relative to the frame $\{S\}$, ${}^s_p\boldsymbol{\omega}$ is the angular velocity of the frame $\{P\}$ relative to the frame $\{S\}$, ${}^o_p\boldsymbol{a}$ is the angular acceleration of the frame $\{P\}$ relative to the frame $\{O\}$. $\boldsymbol{I}_s = {}^s_o\boldsymbol{R}^T\boldsymbol{I}_o\,{}^s_o\boldsymbol{R}$ is the inertia tensor of the end-effector in the frame $\{S\}$, ${}^s_o\boldsymbol{R}$ is the rotation matrix from the frame $\{O\}$ to the frame $\{S\}$, ${}^s_p\boldsymbol{R}$ is the rotation matrix from the frame $\{P\}$ to the frame $\{S\}$. The compensation torque of the catamaran acting on the end-effector can be obtained.

$$\boldsymbol{M}_{ca} = -\boldsymbol{M}_s \qquad (29)$$

The compensation torque obtained by catamaran's movement is simulated and verified. When the frame $\{O\}$ moves under a given trajectory, the compensation torque obtained by Eq. (29) will be compensated to the end-effector. The simulation result is shown in Fig. 4.

Fig. 4 shows the Euler angle change of the end-effector relative to the frame $\{S\}$ and the frame $\{O\}$ relative to the frame $\{S\}$. $\boldsymbol{\theta}_o = [\alpha_o\beta_o\gamma_o]^T$ is the Euler angle of the frame $\{O\}$ relative to the frame $\{S\}$. It can be observed that when $\boldsymbol{\theta}_o$ changes, the change of $\boldsymbol{\theta}$ of the end-effector relative to the frame $\{S\}$ is zero. At this time, the end-effector is stationary with respect to the frame $\{S\}$. The compensation torque calculated by gyroscope and accelerometer can compensate the interference of the catamaran to the end-effector.

IV. CONTROLLER DESIGN

The CDUCSP system has nonlinearity and strong coupling. Moreover, it is necessary to overcome the interference of random water wave on the system and the inertia torque

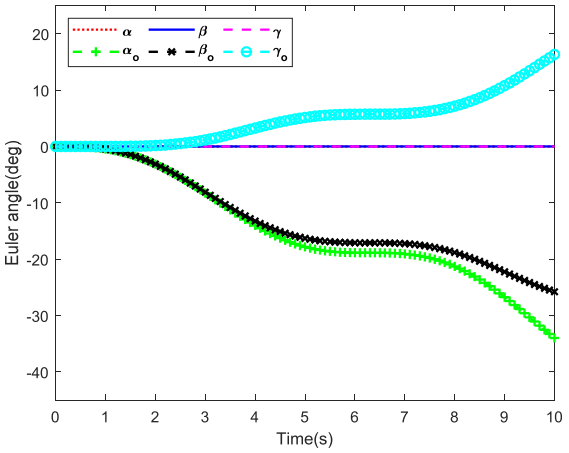

FIGURE 4. Euler angle change.

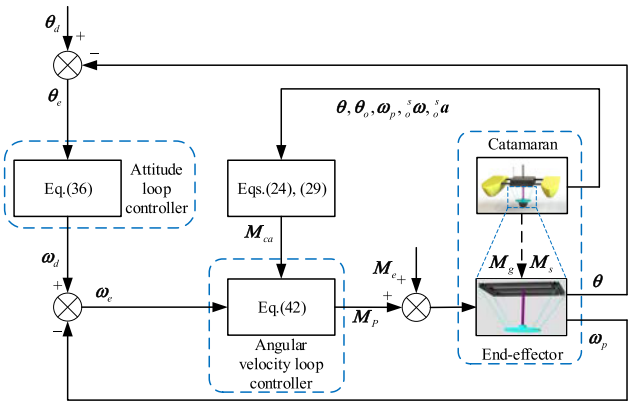

FIGURE 5. Diagram of the proposed DIGFTSMC scheme.

of catamaran acting on the end-effector. To ensure high-precision tracking control of CDUCSP, we propose a novel DIGFTSMC control scheme in this section. The integral function is used to realize the design of sliding mode surface. Furthermore, to further reduce the system chattering, an exponential function is used to design the reaching law.

The DIGFTSMC is composed of an attitude loop and an angular velocity loop. The attitude loop realizes the tracking of the desired attitude angle $\boldsymbol{\theta}_d$ of the end-effector. The angular velocity command $\boldsymbol{\omega}_d$ is used as a virtual control item of the $\boldsymbol{\omega}_p$. The angular velocity loop realizes the tracking of the end-effector $\boldsymbol{\omega}_d$. The system structure of DIGFTSMC is shown in Fig. 5.

Based on the dynamic modeling in section III, the rotational dynamic equation of CDUCSP in the frame $\{P\}$ is

$$\boldsymbol{I}_p\dot{\boldsymbol{\omega}}_p + \boldsymbol{\omega}_{p\times}\boldsymbol{I}_p\boldsymbol{\omega}_p = \boldsymbol{M}_p + \boldsymbol{M}_g + \boldsymbol{M}_e + \boldsymbol{M}_s \qquad (30)$$

where $\boldsymbol{\omega}_{p\times} = \begin{bmatrix} 0 & -\omega_{pz} & \omega_{py} \\ \omega_{pz} & 0 & -\omega_{px} \\ -\omega_{py} & \omega_{px} & 0 \end{bmatrix}$ is the skew-symmetric matrix.

A. ATTITUDE LOOP SLIDING MODE CONTROLLER

The attitude loop controller is used to generate the angular velocity command $\boldsymbol{\omega}_d$. The desired attitude angle is defined

as $\boldsymbol{\theta}_d$, and the attitude angle tracking deviation is $\boldsymbol{\theta}_e = \boldsymbol{\theta}_d - \boldsymbol{\theta}$. In order to improve the convergence speed and achieve $\lim_{t\to\infty} \|\boldsymbol{\theta}_d - \boldsymbol{\theta}\| = 0$, the integral sliding surface of attitude loop controller is described by the following equation

$$\boldsymbol{s}_1 = \boldsymbol{\theta}_e + \int_0^t (K_1 sign^{a_1}(\boldsymbol{\theta}_e) + K_2 sign^{a_2}(\boldsymbol{\theta}_e))dt \quad (31)$$

where, $\boldsymbol{s}_1 \in \Re^3$ is the sliding variable, $K_1, K_2 > 0, a_1 \geq 1, 0 < a_2 < 1$. Further, for the convenience of expression, the following operations are defined

$$sign^a(\theta) = |\theta|^a \, sign(\theta) \quad (32)$$

$$\frac{d}{dt} sign^a(\theta) = a sign^{a-1}(\theta)\dot{\theta} \quad (33)$$

where, *sign* is a sign function. Differentiating Eq. (31) with respect to time, and substituting Eq. (6) into it, we have

$$\begin{aligned}\dot{\boldsymbol{s}}_1 &= \dot{\boldsymbol{\theta}}_e + K_1 sign^{a_1}(\boldsymbol{\theta}_e) + K_2 sign^{a_2}(\boldsymbol{\theta}_e) \\ &= \dot{\boldsymbol{\theta}}_d - \dot{\boldsymbol{\theta}} + K_1 sign^{a_1}(\boldsymbol{\theta}_e) + K_2 sign^{a_2}(\boldsymbol{\theta}_e) \\ &= \dot{\boldsymbol{\theta}}_d - \boldsymbol{J}_P \boldsymbol{\omega}_d + K_1 sign^{a_1}(\boldsymbol{\theta}_e) + K_2 sign^{a_2}(\boldsymbol{\theta}_e) \quad (34)\end{aligned}$$

The form of the exponential reaching law is designed as

$$\dot{\boldsymbol{s}}_1 = -H_1 \boldsymbol{s}_1 - H_2 sign(\boldsymbol{s}_1) \quad (35)$$

where, $H_1, H_2 > 0$, the designed attitude loop control law $\boldsymbol{\omega}_d$ is

$$\begin{aligned}\boldsymbol{\omega}_d = \boldsymbol{J}_p^{-1}[&\dot{\boldsymbol{\theta}}_d + K_1 sign^{a_1}(\boldsymbol{\theta}_e) + K_2 sign^{a_2}(\boldsymbol{\theta}_e) \\ &+ H_1 \boldsymbol{s}_1 + H_2 sign(\boldsymbol{s}_1)] \quad (36)\end{aligned}$$

To prove the correctness of controller convergence, we consider a Lyapunov function as follows

$$V_1 = \frac{1}{2} \boldsymbol{s}_1^T \boldsymbol{s}_1 \quad (37)$$

Differentiating V_1 with respect to time, while substituting Eq. (34) and Eq. (36), we have

$$\begin{aligned}\dot{V}_1 &= \boldsymbol{s}_1^T \dot{\boldsymbol{s}}_1 \\ &= \boldsymbol{s}_1^T (\dot{\boldsymbol{\theta}}_d - \boldsymbol{J}_P \boldsymbol{\omega}_d + K_1 sign^{a_1}(\boldsymbol{\theta}_e) + K_2 sign^{a_2}(\boldsymbol{\theta}_e)) \\ &= \boldsymbol{s}_1^T (-H_1 \boldsymbol{s}_1 - H_2 sign(\boldsymbol{s}_1)) \\ &= -H_1 \|\boldsymbol{s}_1\|^2 - H_2 \sum_{i=1}^{3} |s_{1i}| < 0 \quad (38)\end{aligned}$$

The global asymptotic stability of the attitude loop controller system is determined by the Lyapunov stability theory. So, the tracking deviation of the attitude angle can converge to zero in a finite time.

B. ANGULAR VELOCITY LOOP SLIDING MODE CONTROLLER

The angular velocity tracking deviation is defined as $\boldsymbol{\omega}_e = \boldsymbol{\omega}_d - \boldsymbol{\omega}_p$. To achieve $\lim_{t\to\infty} \|\boldsymbol{\omega}_d - \boldsymbol{\omega}_p\| = 0$, the integral sliding surface of angular velocity loop controller is described by the following equation

$$\boldsymbol{s}_2 = \boldsymbol{\omega}_e + \int_0^t (K_3 sign^{a_3}(\boldsymbol{\omega}_e) + K_4 sign^{a_4}(\boldsymbol{\omega}_e))dt \quad (39)$$

where, $\boldsymbol{s}_2 \in \Re^3$ is the sliding variable, $K_3, K_4 > 0, a_3 \geq 1$, $0 < a_4 < 1$. Differentiating Eq. (39) with respect to time, one can get

$$\begin{aligned}\dot{\boldsymbol{s}}_2 &= \dot{\boldsymbol{\omega}}_e + K_3 sign^{a_3}(\boldsymbol{\omega}_e) + K_4 sign^{a_4}(\boldsymbol{\omega}_e) \\ &= \dot{\boldsymbol{\omega}}_d - \dot{\boldsymbol{\omega}}_p + K_3 sign^{a_3}(\boldsymbol{\omega}_e) + K_4 sign^{a_4}(\boldsymbol{\omega}_e) \quad (40)\end{aligned}$$

The form of the exponential reaching law is designed as

$$\dot{\boldsymbol{s}}_2 = -H_3 \boldsymbol{s}_2 - H_4 sign(\boldsymbol{s}_2) \quad (41)$$

where, $H_3, H_4 > 0$, combining Eqs. (30), (40), (41), the designed angular velocity loop control law $\boldsymbol{M}_p$ is

$$\begin{aligned}\boldsymbol{M}_p = \boldsymbol{I}_p(&\dot{\boldsymbol{\omega}}_d + K_3 sign^{a_3}(\boldsymbol{\omega}_e) + K_4 sign^{a_4}(\boldsymbol{\omega}_e)) \\ &+ H_3 \boldsymbol{s}_2 + H_4 sign(\boldsymbol{s}_2) + \boldsymbol{\omega}_{p\times} \boldsymbol{I}_p \boldsymbol{\omega}_p - \boldsymbol{M}_g + \boldsymbol{M}_{ca} \quad (42)\end{aligned}$$

Substituting Eqs. (27), (30), (42) into Eq. (40), one can get

$$\begin{aligned}\dot{\boldsymbol{s}}_2 &= \dot{\boldsymbol{\omega}}_d - \dot{\boldsymbol{\omega}}_p + K_3 sign^{a_3}(\boldsymbol{\omega}_e) + K_4 sign^{a_4}(\boldsymbol{\omega}_e) \\ &= \dot{\boldsymbol{\omega}}_d + \boldsymbol{I}_p^{-1}(\boldsymbol{\omega}_{p\times} \boldsymbol{I}_p \boldsymbol{\omega}_p - \boldsymbol{M}_p - \boldsymbol{M}_g - \boldsymbol{M}_e - \boldsymbol{M}_s) \\ &\quad + K_3 sign^{a_3}(\boldsymbol{\omega}_e) + K_4 sign^{a_4}(\boldsymbol{\omega}_e) \\ &= -\boldsymbol{I}_p^{-1}(H_3 \boldsymbol{s}_2 + H_4 sign(\boldsymbol{s}_2) + \boldsymbol{M}_e) \quad (43)\end{aligned}$$

To prove the correctness of controller convergence, we consider a Lyapunov function as follows

$$V_2 = \frac{1}{2} \boldsymbol{s}_2^T \boldsymbol{I}_p \boldsymbol{s}_2 \quad (44)$$

Suppose the interference torque $\boldsymbol{M}_e$ is bounded and $H_4 > |\boldsymbol{M}_e|$. Differentiating V_2 with respect to time, while substituting Eq.(43), we have

$$\begin{aligned}\dot{V}_2 &= \boldsymbol{s}_2^T \boldsymbol{I}_p \dot{\boldsymbol{s}}_2 \\ &= \boldsymbol{s}_2^T \boldsymbol{I}_p (-\boldsymbol{I}_p^{-1}(H_3 \boldsymbol{s}_2 + H_4 sign(\boldsymbol{s}_2) + \boldsymbol{M}_e)) \\ &= \boldsymbol{s}_2^T (-H_3 \boldsymbol{s}_2 - H_4 sign(\boldsymbol{s}_2) - \boldsymbol{M}_e) \\ &= -H_3 \|\boldsymbol{s}_2\|^2 - H_4 \sum_{i=1}^{3} |s_{2i}| - \boldsymbol{s}_2^T \boldsymbol{M}_e \\ &< -H_3 \|\boldsymbol{s}_2\|^2 < 0 \quad (45)\end{aligned}$$

The global asymptotic stability of the angular velocity loop controller system is determined by the Lyapunov stability theory. So, the tracking deviation of the angular velocity can converge to zero in a finite time.

C. TENSION SOLUTION ALGORITHM

In order to keep the cable tension within the preset range during the control process, the tension solution algorithm is designed. It can be seen from Eq. (15) and Eq. (20) that the rotational dynamic equations are non-homogeneous equations. The tension $\boldsymbol{T}$ of the four cables is a set of four-dimensional unknown vector. The solution of non-homogeneous equations includes a basic solution system and a special solution, which is

$$\boldsymbol{T} = \boldsymbol{T}_s + \boldsymbol{T}_f \quad (46)$$

where $\boldsymbol{T}_s$ is a special solution, $\boldsymbol{T}_f$ is a basic solution system. Assuming that the minimum pre-tightening force of the cable

is $\boldsymbol{T}_{\min}$ and the maximum allowable tension is $\boldsymbol{T}_{\max}$. $\boldsymbol{T}_s$ is designed as

$$\boldsymbol{T}_s = \frac{\boldsymbol{T}_{\max} + \boldsymbol{T}_{\min}}{2} \tag{47}$$

The solution to the rotational dynamic equation can be written as the addition of $\boldsymbol{T}_s$ and $\boldsymbol{T}_f$. Eq. (20) can be written as

$$\boldsymbol{J}^T(\boldsymbol{T}_s + \boldsymbol{T}_f) = \boldsymbol{M}_p \tag{48}$$

Eq. (48) can be written as

$$\boldsymbol{J}^T\boldsymbol{T}_f = \boldsymbol{M}_p - \boldsymbol{J}^T\boldsymbol{T}_s \tag{49}$$

Since $\boldsymbol{J}^T$ is not a square matrix, that is, the robot has redundant characteristics, there is no inverse matrix for $\boldsymbol{J}^T$. For non-square matrices, we can solve the Moore-Penrose pseudoinverse [51]. Let $\boldsymbol{J}^{T-}$ be the Moore-Penrose pseudoinverse of $\boldsymbol{J}^T$

$$\boldsymbol{J}^{T-} = \boldsymbol{J}(\boldsymbol{J}^T\boldsymbol{J})^{-1} \tag{50}$$

Substituting Eq. (50) into Eq. (49), we can get

$$\boldsymbol{T}_f = \boldsymbol{J}^{T-}(\boldsymbol{M}_p - \boldsymbol{J}^T\boldsymbol{T}_s) \tag{51}$$

Combining Eqs. (46), (50), (51), we have

$$\boldsymbol{T} = \boldsymbol{T}_s + \boldsymbol{J}(\boldsymbol{J}^T\boldsymbol{J})^{-1}(\boldsymbol{M}_p - \boldsymbol{J}^T\boldsymbol{T}_s) \tag{52}$$

So the tension of the cable can be maintained between the preset minimum pre-tightening force and the maximum allowable tension.

The preset minimum pre-tightening force in the paper is $10N$ and the maximum allowable tension is $200N$. The tension values of the four cables do not change much within this range. The cable elasticity has weaker interference to the end-effector when working. And the tension of the cable selected by this paper is far greater than the preset tension value range, so the elastic deformation of the cable can be ignored. Therefore, to facilitate modeling, cable elasticity is not currently considered.

V. SIMULATION ANALYSIS

To verify the validity and advantages of the CDUCSP model design and proposed control strategy, dynamic simulation analysis of the model is carried out. By comparing the simulation with the existing GFTSMC and the traditional SMC, the corresponding simulation results and conclusions are drawn. The GFTSMC control law design can be seen in the APPENDIX.

According to the established coordinate system, the relevant parameters of the CDUCSP model are shown in Table 1:

Since the actual operating conditions of the real model of CDUCSP must be considered, the cable tension must be kept within the preset tension value range. At the same time, the torque acting on the end-effector and the end-effector angular velocity must conform to the actual operating conditions of the model. Therefore, the proposed DIGFTSMC controller parameters should be within a reasonable range.

TABLE 1. Parameters of CDUCSP.

Parameter	Value	Unit
m	5	kg
${}^{p}\boldsymbol{r}$	$[0\ 0\ 30]^T$	mm
${}^{o}\boldsymbol{p}$	$[0\ 0\ 300]^T$	mm
${}^{o}\boldsymbol{b}_1$	$[300\ 200\ 0]^T$	mm
${}^{o}\boldsymbol{b}_2$	$[-300\ 200\ 0]^T$	mm
${}^{o}\boldsymbol{b}_3$	$[-300\ -200\ 0]^T$	mm
${}^{o}\boldsymbol{b}_4$	$[300\ -200\ 0]^T$	mm
${}^{p}\boldsymbol{a}_1$	$[50\ 150\ 25]^T$	mm
${}^{p}\boldsymbol{a}_2$	$[-50\ 150\ 25]^T$	mm
${}^{p}\boldsymbol{a}_3$	$[-50\ -150\ 25]^T$	mm
${}^{p}\boldsymbol{a}_4$	$[50\ -150\ 25]^T$	mm
$\boldsymbol{T}_{\min}$	$[10\ 10\ 10\ 10]^T$	N
$\boldsymbol{T}_{\max}$	$[200\ 200\ 200\ 200]^T$	N
$\boldsymbol{I}_p$	$diag(0.0377\ 0.0043\ 0.0417)$	$\mathrm{kg\cdot m^2}$

TABLE 2. Parameters of controller.

Controller	Parameters	Value
Proposed DIGFTSMC	k_1, k_2, a_1, a_2, H_1, H_2, k_3, k_4, a_3, a_4, H_3, H_4	1, 1, 1.1, 0.9, 1, 65, 1, 1, 1.1, 0.9, 0.3, 0.9
Existing GFTSMC	k_5, k_6, a_5, a_6, H_5, H_6,	20, 1.5, 1.1, 0.9, 100, 200
Conventional SMC	k_7, H_7, H_8	10, 40, 100

The corresponding model simulation convergence time and convergence speed should also be within a reasonable range.

Therefore, the relevant parameters of the proposed DIGFTSMC and existing GFTSMC are shown in Table 2:

Set initial angle $\boldsymbol{\theta} = [0\ 0\ 0]^T$, initial angular velocity $\boldsymbol{\omega}_p = [0\ 0\ 0]^T$. The simulation time lasts for 15 seconds with a fixed step size of 0.001.

Simulation 1: Set the desired motion trajectory of the end-effector is

$$\begin{cases} \alpha = 5\cos t \\ \beta = 5\cos(\pi t) \\ \gamma = 5\cos(\pi t/2) \end{cases} \tag{53}$$

Fig. 6 shows random water wave interference torques. When the significant wave height is 0.25m, it respectively represents the disturbance torque acting on the end-effector

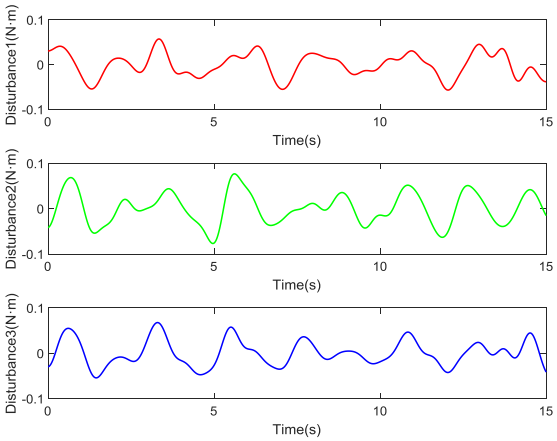

FIGURE 6. Random water wave interference torques along the X_p, Y_p, and Z_p axes.

along the X_p, Y_p, and Z_p axes. The attitude angle tracking of α, β, and γ are shown in Fig. 7. The attitude angle tracking errors of α, β, and γ are shown in Fig. 8. Fig. 7 shows that when the tension value is within the preset range, the three control schemes can ensure good tracking of the desired trajectory. This result effectively demonstrates the correctness of CDUCSP dynamic modeling, random water interference modeling, and catamaran interference modeling. It can be clearly observed from Fig. 7 and Fig. 8 that the proposed DIGFTSMC has better control performance among the three control schemes. Compared with the other two, the proposed control strategy has faster convergence and higher accuracy. The stable tracking error is within $\pm 0.02°$. It is validated that the proposed controller can effectively suppress external interference and has high tracking accuracy.

Fig. 9 shows the four cable tension changes under the DIGFTSMC scheme when the end-effector runs along the desired trajectory. The tensions are all positive, and there is no abnormal mutation point, which meets the preset minimum pre-tightening force and maximum allowable force. The variation of tensions conforms to the actual movement of the end-effector, which proves the rationality of the tension solution algorithm. Fig. 10 and Fig. 11 show the control torque change and angular velocity change of the end-effector along the X_p, Y_p, and Z_p axes under the DIGFTSMC scheme, respectively. It can be seen that there is no sudden change point in the continuous curve change, which is in line with the actual situation of the end-effector movement.

Simulation 2: Set the desired motion trajectory as a step signal, which is specifically expressed as

$$\begin{cases} \alpha = 0, \beta = 0, \gamma = 0, & (0 \le t < 2) \\ \alpha = 5, \beta = 5, \gamma = 5, & (2 \le t \le 15) \end{cases} \tag{54}$$

The external interference torque is the same as Fig. 6. The step response curves of α, β, and γ are shown in Fig. 12. The step response tracking errors of α, β, and γ are shown in Fig. 13. The simulation results show that the step response of the end-effector can effectively track the desired motion

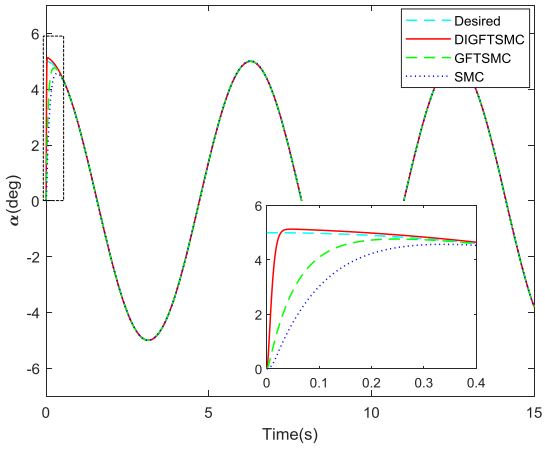

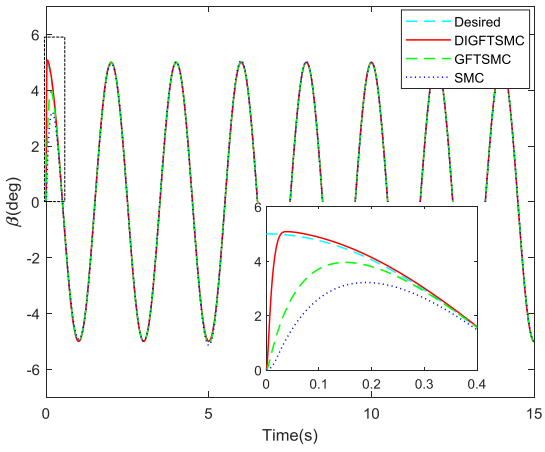

(b)

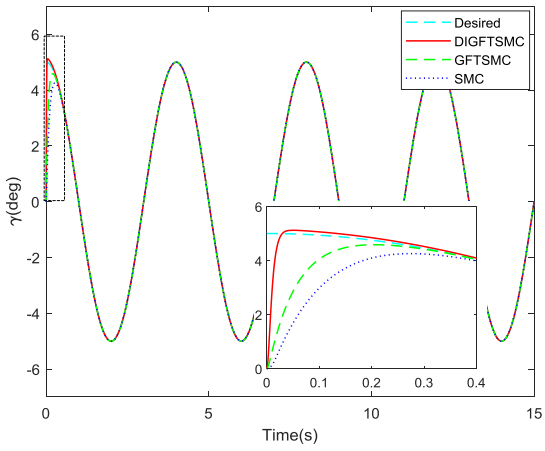

(c)

FIGURE 7. Attitude trajectory tracking of (a) α, (b) β, and (c) γ.

trajectory under external interference. The overshoots of step response are 0.64%, 0.75%, and 0.625%, respectively. When the step response curves reach and stay within $\pm 2\%$ of the

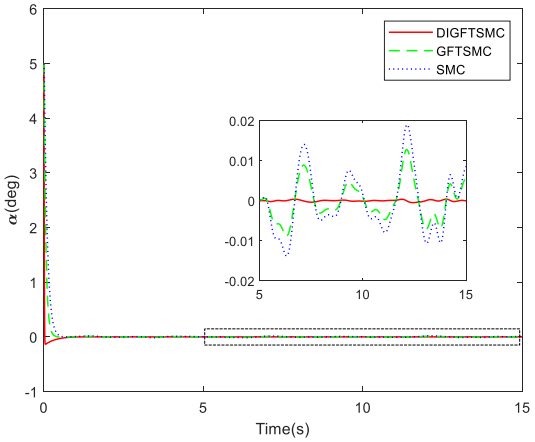

(a)

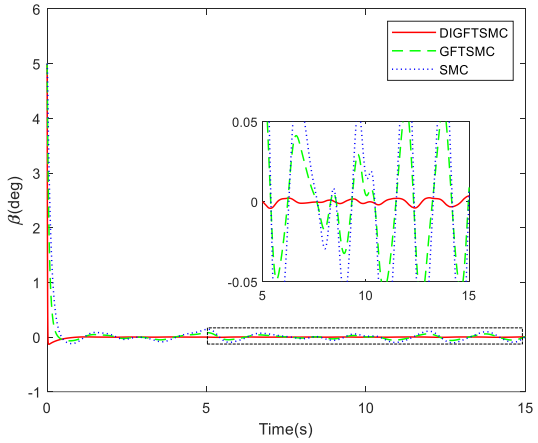

(b)

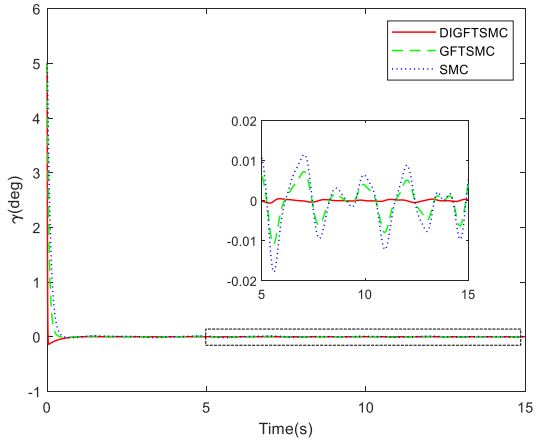

(c)

FIGURE 8. Attitude tracking errors of (a) α, (b) β, and (c) γ.

final value, the settling times are 0.038s, 0.035s, and 0.039s, respectively. The stable tracking error is within $\pm 0.02°$. The results validate that the system has fast dynamic response and small stability error.

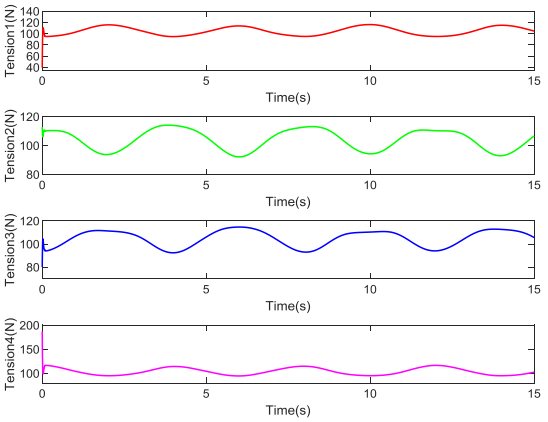

FIGURE 9. Tensions of the four cables with time.

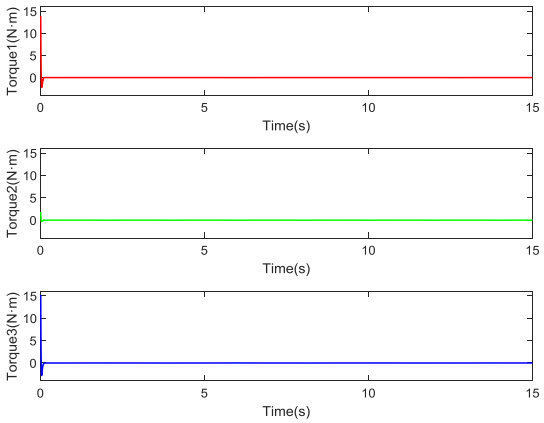

FIGURE 10. Control torque acting on CDUCSP along the X_p, Y_p, and Z_p axes.

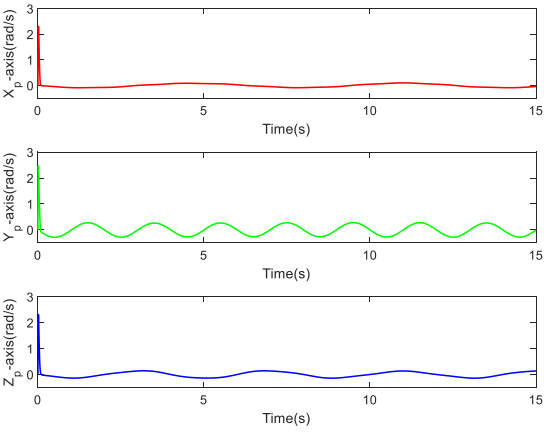

FIGURE 11. Angular velocities along the X_p, Y_p, and Z_p axes.

VI. CONCLUSION

In this paper, a cable-driven parallel platform is proposed for underwater camera stabilization. The designed parallel mechanism driven by four cables realizes the high water-proof requirement of the platform. Aiming at the influence of

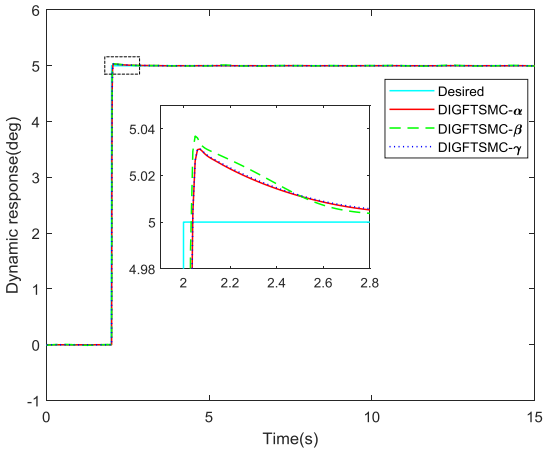

FIGURE 12. Step response of attitude.

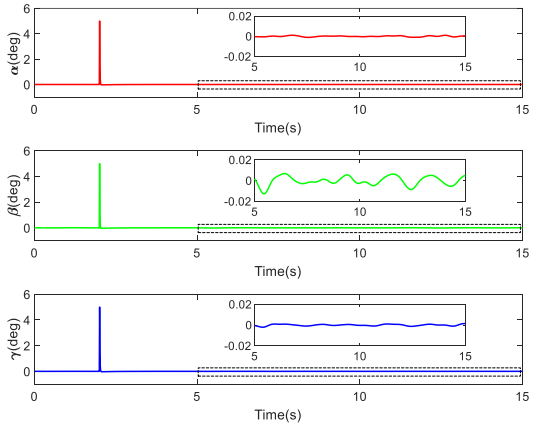

FIGURE 13. Step response tracking errors of attitude.

external water wave interference and catamaran's movement, a more accurate dynamic model is established. And considering the cable tension problem, the tension solution algorithm designed can meet the system requirements. To achieve the accuracy and robustness of trajectory tracking, a DIGFTSMC control strategy is designed. Furthermore, the proposed controller and existing GFTSMC and SMC are co-simulated in dynamics under external interference. The results show that the DIGFTSMC has faster response speed, strong robustness, and has the characteristics of fast finite time convergence and higher tracking accuracy. The rationality and high image stabilization accuracy of CDUCSP are validated. The established CDUCSP can provide a theoretical reference for developing UCSP.

Moreover, the following issues should be considered before the development and practical application of the physical model:

(1) More actual system constraints and uncertainties need to be considered in the controller design, such as the sensor measurement errors.

(2) The optimal tension distribution strategy of each cable needs to be considered more carefully. And the time efficiency of cable tension optimization algorithm also needs to be further studied.

In future work, the above-mentioned problems will be studied and solved. And the CDUCSP physical model will be developed, and its performance will be comprehensively compared and tested in the actual underwater environment.

APPENDIX

The integral sliding surface of GFTSMC is described by the following equation [49], [50]

$$\boldsymbol{s}_3 = \boldsymbol{\omega}_e + K_5 sign^{a_5}(\boldsymbol{\theta}_e) + K_6 sign^{a_6}(\boldsymbol{\theta}_e) \tag{55}$$

where $\boldsymbol{s}_3 \in \Re^3$ is the sliding variable, $K_5, K_6 > 0, a_5 \geq 1$, $0 < a_6 < 1$. The form of the exponential reaching law is designed as

$$\dot{\boldsymbol{s}}_3 = -H_5 \boldsymbol{s}_3 - H_6 sign(\boldsymbol{s}_3) \tag{56}$$

where, $H_5, H_6 > 0$, combining Eqs. (30), (55), (56), the GFTSMC control law $\boldsymbol{M}_p$ is

$$\begin{aligned} \boldsymbol{M}_p = \boldsymbol{I}_p[&\dot{\boldsymbol{\theta}}_e(K_5 a_5 sign^{a_5-1}(\boldsymbol{\theta}_e) + K_6 a_6 sign^{a_6-1}(\boldsymbol{\theta}_e)) \\ &+\dot{\boldsymbol{\omega}}_d + H_5 \boldsymbol{s}_3 + H_6 sign(\boldsymbol{s}_3)] \\ &+\boldsymbol{\omega}_{p\times} \boldsymbol{I}_p \boldsymbol{\omega}_p - \boldsymbol{M}_g + \boldsymbol{M}_{ca} \end{aligned} \tag{57}$$

The integral sliding surface of conventional SMC is described by the following equation [50]

$$\boldsymbol{s}_4 = \boldsymbol{\omega}_e + K_7 \boldsymbol{\theta}_e \tag{58}$$

where $\boldsymbol{s}_4 \in \Re^3$ is the sliding variable, $K_7 > 0$. The form of the exponential reaching law is designed as

$$\dot{\boldsymbol{s}}_4 = -H_7 \boldsymbol{s}_4 - H_8 sign(\boldsymbol{s}_4) \tag{59}$$

where, $H_7, H_8 > 0$, combining Eqs.(30), (58), (59), the conventional SMC control law $\boldsymbol{M}_p$ is

$$\begin{aligned} \boldsymbol{M}_p = \boldsymbol{I}_p(&\dot{\boldsymbol{\omega}}_d + K_7 \dot{\boldsymbol{\theta}}_e + H_7 \boldsymbol{s}_4 + H_8 sign(\boldsymbol{s}_4)) \\ &+ \boldsymbol{\omega}_{p\times} \boldsymbol{I}_p \boldsymbol{\omega}_p - \boldsymbol{M}_g + \boldsymbol{M}_{ca} \end{aligned} \tag{60}$$

REFERENCES

[1] A. Purser, Y. Marcon, S. Dreutter, U. Hoge, B. Sablotny, L. Hehemann, J. Lemburg, B. Dorschel, H. Biebow, and A. Boetius, "Ocean floor observation and bathymetry system (OFOBS): A new towed camera/sonar system for deep-sea habitat surveys," *IEEE J. Ocean. Eng.*, vol. 44, no. 1, pp. 87–99, Jan. 2019.

[2] J. Aguzzi, C. Doya, S. Tecchio, F. C. De Leo, E. Azzurro, C. Costa, V. Sbragaglia, J. D. Río, J. Navarro, H. A. Ruhl, J. B. Company, P. Favali, A. Purser, L. Thomsen, and I. A. Catalán, "Coastal observatories for monitoring of fish behaviour and their responses to environmental changes," *Rev. Fish Biol. Fisheries*, vol. 25, no. 3, pp. 463–483, May 2015.

[3] M. Cappo, G. Déath, and P. Speare, "Inter-reef vertebrate communities of the great barrier reef marine park determined by baited remote underwater video stations," *Mar. Ecol. Prog. Ser.*, vol. 350, pp. 209–221, Nov. 2007.

[4] J. Aguzzi, N. Iveša, M. Gelli, C. Costa, A. Gavrilovic, N. Cukrov, M. Cukrov, N. Cukrov, D. Omanovic, M. Štifanić, S. Marini, M. Piria, E. Azzurro, E. Fanelli, and R. Danovaro, "Ecological video monitoring of marine protected areas by underwater cabled surveillance cameras," *Mar. Policy*, vol. 119, Sep. 2020, Art. no. 104052.

[5] Q. Jiang and V. Kumar, "The inverse kinematics of cooperative transport with multiple aerial robots," *IEEE Trans. Robot.*, vol. 29, no. 1, pp. 136–145, Feb. 2013.

[6] H. Wei, Y. Qiu, and J. Yang, "An approach to evaluate stability for cable-based parallel camera robots with hybrid tension-stiffness properties," *Int. J. Adv. Robot. Syst.*, vol. 12, no. 12, p. 185, Dec. 2015.

[7] J. Niu, Q. Yang, G. Chen, and R. Song, "Nonlinear disturbance observer based sliding mode control of a cable-driven rehabilitation robot," in *Proc. Int. Conf. Rehabil. Robot. (ICORR)*, London, U.K., Jul. 2017, pp. 664–669.

[8] C.-T. Chen, W.-Y. Lien, C.-T. Chen, M.-J. Twu, and Y.-C. Wu, "Dynamic modeling and motion control of a cable-driven robotic exoskeleton with pneumatic artificial muscle actuators," *IEEE Access*, vol. 8, pp. 149796–149807, Aug. 2020.

[9] A. Ghaffar and M. Hassan, "Study on cable based parallel manipulator systems for subsea applications," in *Proc. 3rd Int. Conf. Mech. Eng. Mechtron.*, Prague, Czech Republic, Aug. 2014, pp. 1–8.

[10] M. M. Horoub, M. Hassan, and M. A. Hawwa, "Workspace analysis of a Gough-Stewart type cable marine platform subjected to harmonic water waves," *Mech. Mach. Theory*, vol. 120, pp. 314–325, Feb. 2018.

[11] G. El-Ghazaly, M. Gouttefarde, and V. Creuze, "Hybrid cable-thruster actuated underwater vehicle-manipulator systems: A study on force capabilities," in *Proc. IEEE/RSJ Int. Conf. Intell. Robots Syst. (IROS)*, Hamburg, Germany, Sep. 2015, pp. 1672–1678.

[12] D. Debruyn, R. Zufferey, S. F. Armanini, C. Winston, A. Farinha,Y. Jin, and M. Kovac, "MEDUSA: A multi-environment dual-robot for underwater sample acquisition," *IEEE Robot. Autom. Lett.*, vol. 5, no. 3, pp. 4564–4571, Jul. 2020.

[13] M. Horoub and M. Hawwa, "Influence of cables layout on the dynamic workspace of a six-DOF parallel marine manipulator," *Mech. Mach. Theory*, vol. 129, pp. 191–201, Nov. 2018.

[14] H. Yuan, E. Courteille, M. Gouttefarde, and P.-E. Hervé, "Vibration analysis of cable-driven parallel robots based on the dynamic stiffness matrix method," *J. Sound Vibrat.*, vol. 394, pp. 527–544, Apr. 2017.

[15] J. Begey, L. Cuvillon, M. Lesellier, M. Gouttefarde, and J. Gangloff, "Dynamic control of parallel robots driven by flexible cables and actuated by position-controlled winches," *IEEE Trans. Robot.*, vol. 35, no. 1, pp. 286–293, Feb. 2019.

[16] J. Hui, M. Pan, R. Zhao, L. Luo, and L. Wu, "The closed-form motion equation of redundant actuation parallel robot with joint friction: An application of the Udwadia–Kalaba approach," *Nonlinear Dyn.*, vol. 93, no. 2, pp. 689–703, Jul. 2018.

[17] M. Carricato, "Direct geometrico-static problem of underconstrained cable-driven parallel robots with three cables," *J. Mech. Robot.*, vol. 5, no. 3, Aug. 2013, Art. no. 031002.

[18] Y.-F. Lu, D.-P. Fan, H. Liu, and M. Hei, "Transmission capability of precise cable drive including bending rigidity," *Mech. Mach. Theory*, vol. 94, pp. 132–140, Dec. 2015.

[19] H. Li, W. Liu, K. Wang, K. Kawashima, and E. Magid, "A cable-pulley transmission mechanism for surgical robot with backdrivable capability," *Robot. Comput.-Integr. Manuf.*, vol. 49, pp. 328–334, Feb. 2018.

[20] J. Wang, Z. Qi, and G. Wang, "Hybrid modeling for dynamic analysis of cable-pulley systems with time-varying length cable and its application," *J. Sound Vib.*, vol. 406, pp. 277–294, Oct. 2017.

[21] J. Du and S. K. Agrawal, "Dynamic modeling of cable-driven parallel manipulators with distributed mass flexible cables," *J. Vibrat. Acoust.*, vol. 137, no. 2, pp. 1–8, Apr. 2015.

[22] B. K. Sarkar, "Modeling and validation of a 2-DOF parallel manipulator for pose control application," *Robot. Comput.-Integr. Manuf.*, vol. 50, pp. 234–241, Apr. 2018.

[23] J. Guo, H. He, and C. Sun, "Analysis of the performance of aerial work platform working device based on virtual prototype and finite element method," *Energy Proc.*, vol. 104, pp. 568–573, Dec. 2016.

[24] R. J. Caverly and J. R. Forbes, "Dynamic modeling and noncollocated control of a flexible planar cable-driven manipulator," *IEEE Trans. Robot.*, vol. 30, no. 6, pp. 1386–1397, Dec. 2014.

[25] H. Jamshidifar, A. Khajepour, B. Fidan, and M. Rushton, "Vibration regulation of kinematically constrained cable-driven parallel robots with minimum number of actuators," *IEEE/ASME Trans. Mechatronics*, vol. 25, no. 1, pp. 21–31, Feb. 2019.

[26] H. Jamshidifar, M. Rushton, and A. Khajepour, "A reaction-based stabilizer for nonmodel-based vibration control of cable-driven parallel robots," *IEEE Trans. Robot.*, vol. 37, no. 2, pp. 667–674, Apr. 2021.

[27] M. Rushton, H. Jamshidifar, and A. Khajepour, "Multiaxis reaction system (MARS) for vibration control of planar cable-driven parallel robots," *IEEE Trans. Robot.*, vol. 35, no. 4, pp. 1039–1046, Aug. 2019.

[28] Y. Su, Y. Qiu, and P. Liu, "The continuity and real-time performance of the cable tension determining for a suspend cable-driven parallel camera robot," *Adv. Robot.*, vol. 29, no. 12, pp. 743–752, Jun. 2015.

[29] P. H. Borgstrom, B. L. Jordan, B. J. Borgstrom, M. J. Stealey, G. S. Sukhatme, M. A. Batalin, and W. J. Kaiser, "NIMS-PL: A cable-driven robot with self-calibration capabilities," *IEEE Trans. Robot.*, vol. 25, no. 5, pp. 1005–1015, Oct. 2009.

[30] P. H. Borgstrom, B. L. Jordan, G. S. Sukhatme, M. A. Batalin, and W. J. Kaiser, "Rapid computation of optimally safe tension distributions for parallel cable-driven robots," *IEEE Trans. Robot.*, vol. 25, no. 6, pp. 1271–1281, Dec. 2009.

[31] R. J. Caverly and J. R. Forbes, "Flexible cable-driven parallel manipulator control: Maintaining positive cable tensions," *IEEE Trans. Control Syst. Technol.*, vol. 26, no. 5, pp. 1874–1883, Sep. 2018.

[32] G. El-Ghazaly, M. Gouttefarde, and V. Creuze, "Adaptive terminal sliding mode control of a redundantly-actuated cable-driven parallel manipulator: CoGiRo," in *Cable-Driven Parallel Robots*, vol. 32. Cham, Switzerland: Springer, Aug. 2015, pp. 179–200.

[33] B. Zi, B. Wang, and D. Wang, "Design and analysis of a novel cable-actuated palletizing robot," *Int. J. Adv. Robot. Syst.*, vol. 14, no. 6, pp. 1–12, Nov. 2017.

[34] M. Jafari and S. Mobayen, "Second-order sliding set design for a class of uncertain nonlinear systems with disturbances: An LMI approach," *Math. Comput. Simul.*, vol. 156, pp. 110–125, Feb. 2019.

[35] Q. Chen, B. Zi, Z. Sun, Y. Li, and Q. Xu, "Design and development of a new cable-driven parallel robot for waist rehabilitation," *IEEE/ASME Trans. Mechatronics*, vol. 24, no. 4, pp. 1497–1507, Aug. 2019.

[36] C.-D. Li, J.-Q. Yi, Y. Yu, and D.-B. Zhao, "Inverse control of cable-driven parallel mechanism using type-2 fuzzy neural network," *Acta Autom. Sin.*, vol. 36, no. 3, pp. 459–464, Mar. 2010.

[37] H. Jamshidifar, S. Khosravani, B. Fidan, and A. Khajepour, "Vibration decoupled modeling and robust control of redundant cable-driven parallel robots," *IEEE/ASME Trans. Mechatronics*, vol. 23, no. 2, pp. 690–701, Apr. 2018.

[38] H. Jia, W. Shang, F. Xie, B. Zhang, and S. Cong, "Second-order sliding-mode-based synchronization control of cable-driven parallel robots," *IEEE/ASME Trans. Mechatronics*, vol. 25, no. 1, pp. 383–394, Feb. 2020.

[39] A. Benamor and H. Messaoud, "Robust adaptive sliding mode control for uncertain systems with unknown time-varying delay input," *ISA Trans.*, vol. 79, pp. 1–12, Aug. 2018.

[40] M. Firouzi, M. Nasiri, S. Mobayen, and G. B. Gharehpetian, "Sliding mode controller-based BFCL for fault ride-through performance enhancement of DFIG-based wind turbines," *Complexity*, vol. 2020, pp. 1–12, May 2020.

[41] R. de Rijk, M. Rushton, and A. Khajepour, "Out-of-plane vibration control of a planar cable-driven parallel robot," *IEEE/ASME Trans. Mechatronics*, vol. 23, no. 4, pp. 1684–1692, Aug. 2018.

[42] A. Modiri and S. Mobayen, "Adaptive terminal sliding mode control scheme for synchronization of fractional-order uncertain chaotic systems," *ISA Trans.*, vol. 105, pp. 33–50, Oct. 2020.

[43] A. Bartoszewicz and P. Latosiński, "Discrete time sliding mode control with reduced switching—A new reaching law approach," *Int. J. Robust Nonlinear Control*, vol. 26, no. 1, pp. 47–68, Jan. 2016.

[44] Y. Y. Wang, J. W. Chen, F. Yan, K. W. Zhu, and B. Chen, "Adaptive super-twisting fractional-order nonsingular terminal sliding mode control of cable-driven manipulators," *ISA Trans.*, vol. 86, no. 3, pp. 163–180, Mar. 2019.

[45] H. Yan, X. Zhou, H. Zhang, F. Yang, and Z. Wu, "A novel sliding mode estimation for microgrid control with communication time delays," *IEEE Trans. Smart Grid*, vol. 10, no. 2, pp. 1509–1520, Mar. 2019.

[46] W. Gao and J. C. Hung, "Variable structure control of nonlinear systems: A new approach," *IEEE Trans. Ind. Electron.*, vol. 40, no. 1, pp. 45–55, Feb. 1993.

[47] C. Mu and H. He, "Dynamic behavior of terminal sliding mode control," *IEEE Trans. Ind. Electron.*, vol. 65, no. 4, pp. 3480–3490, Apr. 2018.

[48] S. A. Khalilpour, R. Khorrambakht, M. J. Harandi, H. D. Taghirad, and P. Cardou, "Cascade terminal sliding mode control of a deployable cable driven robot," in *Proc. Int. Conf. Control, Instrum. Autom. (ICCIA)*, Sanandaj, Iran, Oct. 2019, pp. 1–6.

[49] C. U. Solis, J. B. Clempner, and A. S. Poznyak, "Fast terminal sliding-mode control with an integral filter applied to a Van der Pol oscillator," *IEEE Trans. Ind. Electron.*, vol. 64, no. 7, pp. 5622–5628, Jul. 2017.

[50] M. Van, M. Mavrovouniotis, and S. S. Ge, "An adaptive backstepping nonsingular fast terminal sliding mode control for robust fault tolerant control of robot manipulators," *IEEE Trans. Syst. Man Cybern., Syst.*, vol. 49, no. 7, pp. 1448–1458, Jan. 2018.
[51] X. Yu and M. Zhihong, "Fast terminal sliding-mode control design for nonlinear dynamical systems," *IEEE Trans. Circuits Syst. I, Fundam. Theory Appl.*, vol. 49, no. 2, pp. 261–264, Feb. 2002.
[52] Y. Wang, K. Zhu, F. Yan, and B. Chen, "Adaptive super-twisting nonsingular fast terminal sliding mode control for cable-driven manipulators using time-delay estimation," *Adv. Eng. Softw.*, vol. 128, pp. 113–124, Feb. 2019.
[53] S. Zaare and M. R. Soltanpour, "Adaptive fuzzy global coupled nonsingular fast terminal sliding mode control of *n*-rigid-link elastic-joint robot manipulators in presence of uncertainties," *Mech. Syst. Signal Process.*, vol. 163, Jan. 2022, Art. no. 108165.
[54] J.-J. Xiong and G.-B. Zhang, "Global fast dynamic terminal sliding mode control for a quadrotor UAV," *ISA Trans.*, vol. 66, pp. 233–240, Jan. 2017.
[55] T. N. Truong, A. T. Vo, and H.-J. Kang, "A backstepping global fast terminal sliding mode control for trajectory tracking control of industrial robotic manipulators," *IEEE Access*, vol. 9, pp. 31921–31931, Feb. 2021.
[56] M. Van, S. S. Ge, and H. Ren, "Finite time fault tolerant control for robot manipulators using time delay estimation and continuous nonsingular fast terminal sliding mode control," *IEEE Trans. Cybern.*, vol. 47, no. 7, pp. 1681–1693, Jul. 2017.
[57] K. M. Lynch and F. C. Park, *Modern Robotics: Mechanics, Planning, and Control*. Cambridge, U.K.: Cambridge Univ. Press, 2017.
[58] T. Perez, *Ship Motion Control: Course Keeping and Roll Reduction Using Rudder and Fins*. London, U.K.: Springer-Verlag, 2005, pp. 10–65.
[59] F. P. Arribas and J. A. C. Fernández, "Strip theories applied to the vertical motions of high speed crafts," *Ocean Eng.*, vol. 33, nos. 8–9, pp. 1214–1229, Jun. 2006.

ZHIQI ZHAO received the B.S. degree in measurement and control technology and instruments from Henan University, China, in 2019, where he is currently pursuing the M.S. degree in control science and engineering. His research interests include parallel robots, cable-driven robots, and sliding mode control.

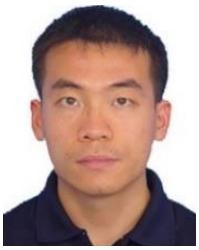

LEI ZHANG received the B.S. degree in mechatronics engineering from Tianjin University, Tianjin, China, in 2003, and the M.S. and Ph.D. degrees in mechatronics engineering from Harbin Institute of Technology, Harbin, China, in 2005 and 2009, respectively.

He is currently an Associate Professor in measurement and control engineering with the School of Physics and Electronics, Henan University, Kaifeng, China. His research interests include robot control, real-time simulation, and virtual reality.

HAIJIAO NAN received the B.S. degree from the University of Science and Technology Beijing, China, in 2018. He is currently pursuing the M.S. degree with Henan University. His research interest includes sliding mode control.

BINBIN WANG received the B.S. degree in measurement and control technology and instruments from Henan University, China, in 2018, where she is currently pursuing the M.S. degree in optical engineering. Her research interests include electromechanical control systems and simulation.